

UCSF

UC San Francisco Electronic Theses and Dissertations

Title

Pharmacokinetics and Biodistribution of ⁸⁹Zr-Df-PEG40 Nanoparticles in Xenograft Tumor Models using micro PET/CT

Permalink

<https://escholarship.org/uc/item/5fj580q6>

Author

Trusz, Guillaume

Publication Date

2018

Peer reviewed|Thesis/dissertation

Pharmacokinetics and Biodistribution of ^{89}Zr -Df-PEG40
Nanoparticles in Xenograft Tumor Models using micro PET/CT

by

Guillaume Trusz

THESIS

Submitted in partial satisfaction of the requirements for the degree of

MASTER OF SCIENCE

in

Biomedical Imaging

in the

GRADUATE DIVISION

Acknowledgements

I dedicate this thesis to my family and friends, without whom this would have never been possible.

I would like to thank Dr. Henry VanBrocklin for providing me the opportunity to complete this wonderful project and contribute to the scientific community. I am very thankful for having had an amazing research mentor, Dr. Denis Beckford Vera, who assisted me throughout my thesis project and who made this a truly memorable experience. Thank you to my other committee members, Dr. Benjamin Franc and Dr. John Kurhanewicz, for providing support and advice throughout this process. In addition, the completion of this project would not have been possible without the assistance and expertise of Tony Huynh. I am extremely honored to have learned from and worked alongside such incredible individuals at UCSF.

I would like to thank my parents, who encouraged and motivated me every step of the way. Moreover, thank you to the 2018 MSBI Class for having made this an unforgettable school year.

Pharmacokinetics and Biodistribution of ⁸⁹Zr-Df-PEG40 Nanoparticles in Xenograft Tumor Models using micro PET/CT

Guillaume Trusz

Abstract

One of the challenges that physicians face is the uncertainty that their therapy of choice will be effective. A reason why therapeutic treatments often fall short in efficacy remains their limited presence and accumulation at the intended site of action. This challenge may be overcome by utilizing non-invasive molecular imaging. Attaching a radiolabel to the therapeutic, one may assess whether or not a drug accumulates at its target site, which may then allow one to more effectively predict whether patients may benefit from the treatment, thus offering patients a form of personalized medicine. **Methods:** Using a Zr-89 radionuclide and μ PET/CT imaging technology, we assessed the pharmacokinetics (PK) of a novel chemotherapy tagged nanoparticle within various murine models engrafted with cell-line derived xenografts and patient-derived xenograft (PDX) tumors. Two other, non-therapeutic, versions of the nanoparticle were also radiolabeled and imaged so as to determine their potential as surrogate imaging probes for the therapeutic version. Tumor bearing mice were injected with 150 – 200 μ Ci of the Zr-89 labeled nanoparticles. Serial images were taken at 1, 24, 48, 72, 96, and 216 hours post-injection. Tumor and organ accumulation of the tracer were determined from the mouse μ PET images. After the last imaging time-point, mice were euthanized and tumor, blood, and organs were weighted and counted. The percent injected dose per gram (%ID/g) of tissue was determined. **Results:** Nanoparticle radiolabeling was greater than 90% yield and 99% purity. μ PET/CT time activity curves (TACs) showed very similar PK trends between the therapeutic and non-therapeutic nanoparticles. A steady accumulation followed by a plateauing of the nanoparticle concentrations within the growing tumors, as well as a clearance from all of the major organs (brain, heart, liver,

and kidneys) was noted. Tumor maximum %ID/mL (5.81 – 18.14) occurred between the 72 and 96 hour time points, and ex vivo BioD experiments confirmed all of our in vivo PK findings ($P > 0.05$). **Conclusion:** Similar PK and BioD patterns between the therapeutic and non-therapeutic versions of the nanoparticle have validated that the imaging probes can in fact be used to predict the uptake and accumulation of the therapeutic nanoparticle.

Table of Contents

Introduction.....	1
Methods.....	7
Results.....	11
Discussion.....	21
Conclusion.....	27
References.....	28

List of Figures

Figure 1: Sequential steps of tumor angiogenesis.....	3
Figure 2: Vascular hyper-permeability.....	3
Figure 3: EPR effect.....	4
Figure 4: Structure of the nanoparticles.....	5
Figure 5: Structure of the three different versions of the nanoparticle assessed in these pre-clinical studies.	7
Figure 6: iTLC and HPLC chromatograms.....	11
Figure 7: PK of ^{89}Zr –Df-PEG40-(SN-38) ₃ in a mouse bearing an MX-1 xenograft tumor.....	12
Figure 8: TACs for nanoparticle injections in mice bearing MX-1 tumors.....	13
Figure 9: TACs for nanoparticle injections in mice bearing HT-29 tumors.....	14
Figure 10: Major organ TACs.....	15
Figure 11: Combined MX-1 and HT-29 tumor TACs.....	16
Figure 12: Combined TACs by nanoparticle type.....	17
Figure 13: Combined TACs by tumor type.....	17
Figure 14: Ex vivo BioD (%ID/g).....	18
Figure 15: Ex vivo BioD (%ID/organ).....	19
Figure 16: AMIDE ROI ($\mu\text{PET}/\text{CT}$) versus Hidex (BioD) tumor data comparison.....	20
Figure 17: TACs for nanoparticle injections in mice bearing a pancreatic PDX tumor.....	21

*Figures 1 and 2 were reproduced with permission [12].

Introduction

Cancer remains one of the deadliest diseases in the world, with a 30 – 40% risk of developing some form of the disease over one's lifetime. Chemotherapy, which targets cancer cells, remains the most prescribed treatment. However, due to its nonspecific nature, chemotherapy also accumulates within healthy cells. Achieving pharmacologically active concentrations of the therapeutic within tumor cells oftentimes come at the expense of whole body toxicity [1]. This of course causes oncology patients to experience a wide range of adverse effects, such as nausea, vomiting, alopecia, and immune suppression [2]. In recent years, new chemotherapy delivery strategies have evolved, taking advantage of a cancerous tumor's aberrant vascular morphology all the while minimizing the therapy's systemic toxicity.

Once a tumor reaches a certain size, in order to retain its high proliferation and cellular division rate, it will have to develop a mechanism to gain access to a nutrient supply. The presence of hypoxia, induced by inadequate perfusion, will lead to the enhanced expression and stabilization (via phosphorylation) of the hypoxia-inducible factor 1 alpha (HIF1 α). HIF1 α will then dimerize with HIF1 β , creating a viable HIF transcription factor [3], which can directly act upon various downstream promoter sequences, including that of the vascular endothelial growth factor (VEGF). It has been reported that in tumors as small as 1 – 2 mm³, VEGF will be expressed, stimulating angiogenesis [4]. The first vessels to form are often referred to as mother vessels, and several ensuing feeder arteries and draining veins steadily develop [5]. Neovascularization provides the tumor the benefit of a constant, nutrient rich source, all the while carrying away some of the cellular wastes as well as facilitating future metastasis.

As opposed to normal healthy vasculature, newly formed blood vessels within the tumor microenvironment are often characterized by an abnormal morphology: extremely convoluted vessels with poor cellular organization. The drastic upregulation of VEGF, which is often expressed in relatively low levels in healthy tissues, has a direct impact on vascular endothelial cell migration and phenotype (Figure 1). Moreover, local immune cells also affected by the hypoxic stress, such as tumor-associated macrophages, play a key role in vascular dysfunction [6, 7]. The transcription factor formed from HIF1 α stabilization in immune cells will interact with nuclear factor - kappa B (NF- κ B). This interaction leads to the production of various pro-inflammatory cytokines, such as tumor necrosis factor - alpha (TNF α), setting in motion an intrinsic inflammatory cascade [8]. TNF α has been known to impact endothelial cell tight junctions [9], as well as affect microtubule arrangement within cadherin-based junctions [10], leading to endothelial barrier dysfunction and ultimately vascular hyper-permeability (Figure 2). A tumor's vascular endothelial pore size typically ranges from 12 to 700 nm, much wider than the healthy vascular pore size of ≤ 12 nm. Enlarged intercellular pores, sometimes referred to as endothelial fenestrations, as well as other vascular abnormalities, are likely responsible for the hemorrhage often seen in tumors in the form of blood lakes, and are indicative of disease progression and ultimately a worse clinical prognosis [11].

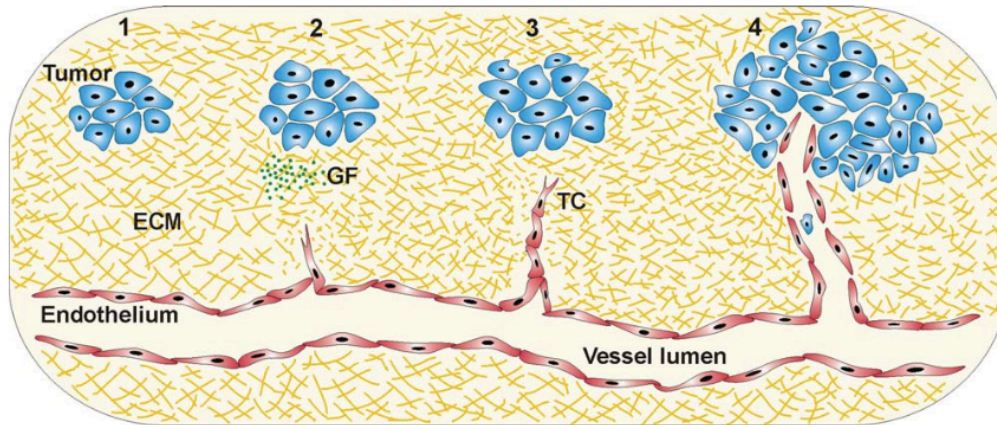


Figure 1: Sequential steps of tumor angiogenesis. Step 1, the growing tumor quickly outgrows its initial nutrient and oxygen source. Step 2, extensive hypoxia within the tumor microenvironment leads to the production and excretion of angiogenic growth factors (GF), stimulating local vasculature. Step 3, endothelial cells adopt a tip cell (TC) phenotype and migrate towards the hypoxic microenvironment. Step 4, newly formed blood vessels connect the tumor to the body's circulatory system, providing the tumor with ample nutrients and oxygen as well as a metastatic route [12].

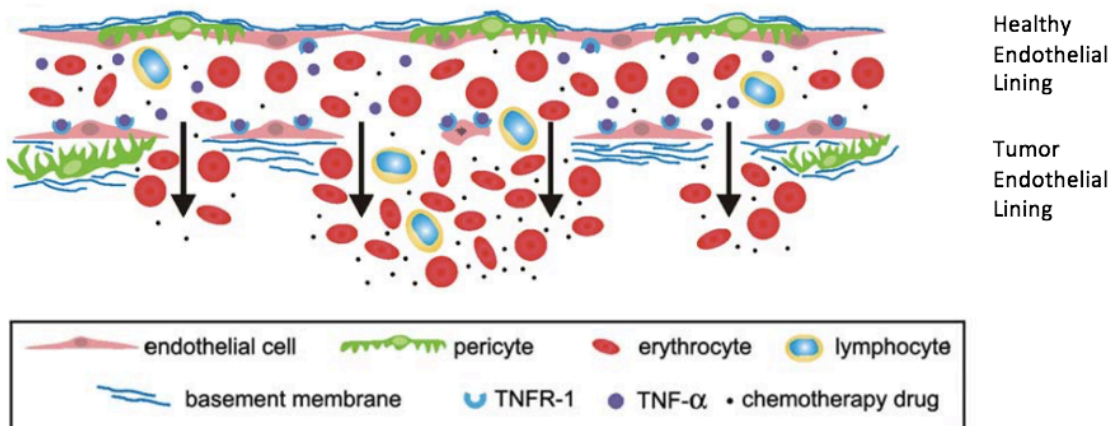


Figure 2: Vascular hyper-permeability. One can observe an increase in endothelial pore size, as well as abnormalities within the pericyte and basement membrane layers of the tunica intima in the arterial vessel walls. These abnormalities synergistically contribute to the leakiness of the tumorous blood vessels. Although predominantly expressed by local immune cells, certain cancer cells have also been reported to express modest levels of $TNF\alpha$, further promoting this vascular dysfunction [12].

Nevertheless, such a large distribution in pore size can be taken advantage of for delivery of novel nanocarriers (nanoparticles carrying the chemotherapy). This hyper-permeable physiologic characteristic gives rise to the enhanced permeability and retention (EPR) effect noted in various tumors [13]. Nanotherapies can easily diffuse through the enlarged pores of the newly formed vessels, accumulating within the tumor's interstitial space, and efflux from the tumor at a dramatically reduced rate due to poor lymphatic drainage (Figure 3).

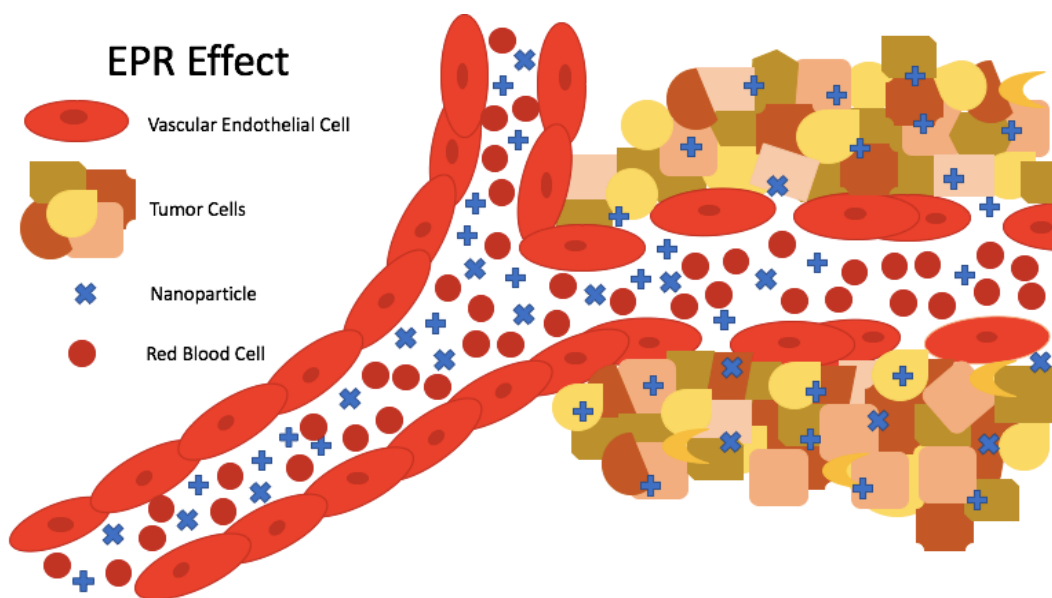


Figure 3: EPR effect. Note significant accumulation of the nanoparticle within the growing tumor due to enlarged vascular endothelial pores combined with poor lymphatic drainage of the tumor microenvironment.

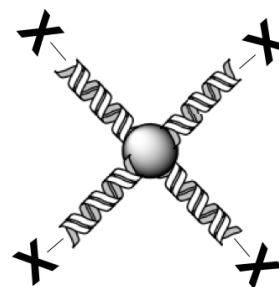
Nanoparticles are designed to passively target a growing tumor but also to prevent the activation of the affiliated chemotherapeutic while in the bloodstream. Delivery through extravasation into tumors followed by the release of the therapeutic (via tumor specific cues) enhances the drug's treatment profile [14]. This delivery mechanism helps overcome some of the limitations of traditional chemotherapy treatments. Encapsulation of the therapeutic within the

nanoparticle core or linkage to the particle's exterior, acts as a form of controlled drug release, and thus limits systemic toxicity [15]. In addition, the nanoparticle's larger size, relative to the size of the small molecule chemotherapeutic, should prevent it from crossing healthy endothelial pores. This would not only result in limited healthy organ accumulation but also hopefully eliminate some of the more uncomfortable side effects affiliated with traditional chemotherapy treatment [16].

Over the past months, we have been assessing the EPR effect of a novel nanoparticle developed by ProLynx, LLC. The nanoparticle consists of a single carbon atom core with four affiliated poly-ethylene glycol (PEG) arms (Figure 4). The versatility of the PEG arms on this star-shaped nanoparticle provides the structure to attach small molecule therapeutics and molecular imaging tags, including optical imaging labels as well as radiolabels. This enables the possibility of assessing and quantifying the nanoparticle's pharmacokinetics (PK) and biodistribution (BioD) within the body.

Figure 4: Structure of the nanoparticle.

The "X" designates the affiliated chemotherapy or imaging tags at the ends of the PEG arms.



Heterogeneous vascular morphologies exist in different regions of the same tumor, different metastases, and even different tumor types. As a result, one cannot expect to find a "one size fits all" nanotherapy [17]. Nevertheless, imaging diagnostic technology via radiolabel allows for a non-invasive assessment of the particle's distribution and tumor accumulation. Thus, if the

therapeutic nanoparticle molecule accumulates in the tumor, the likelihood of an efficacious outcome may be higher.

Previous preclinical studies have shown successful uptake of this novel nanoparticle within various human xenograft tumors. In this study, complete PK studies were performed on three nanoparticle constructs in two xenograft models. In addition, one of the constructs was assessed in a patient derived xenograft (PDX) model, which is more representative of human tumors in an animal model [18].

Using a ^{89}Zr label and micro - positron emission tomography - computed tomography ($\mu\text{PET-CT}$) imaging technology platform, the PK and BioD of the novel nanoparticle was assessed in various pre-clinical models. ^{89}Zr is an ideal radioisotope for labeling and studying nanoparticles as well as other biologically active molecules due to its relatively long half-life ($t_{1/2} = 78.4$ hr) and low energy positron emission (395 keV) [19]. The goal of these studies is to not only evaluate the EPR of the novel nanoparticle within various tumor types, but also to better understand the difference in accumulation patterns between different versions of the nanoparticle (one with the affiliated chemotherapeutic ^{89}Zr -Df-PEG40-(SN-38)₃, and two without ^{89}Zr -Df-PEG40, ^{89}Zr -Df₄-PEG40); (Figure 5). We hypothesize that the imaging probes ^{89}Zr -Df-PEG40 and ^{89}Zr -Df₄-PEG40 have the potential to accumulate within various tumors and could be an effective EPR marker and surrogate for the therapeutic version of this nanoparticle, ^{89}Zr -Df-PEG40-(SN-38)₃.

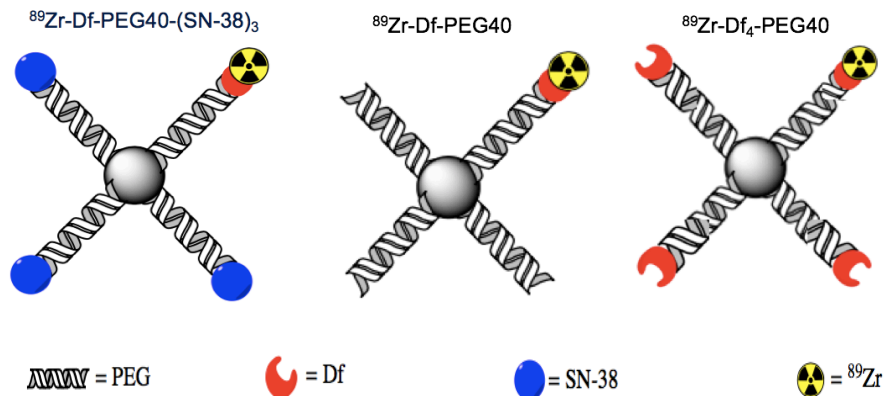


Figure 5: Structure of the three different versions of the nanoparticle to be assessed in these pre-clinical studies. The rightmost nanoparticle, which has four Dfs attached to the various PEG arms, has the potential to have one, two, three, or four zirconium radiolabels.

Methods

A. Radiolabeling

In a centrifuge tube, 10 μL of 1M sodium carbonate (Sigma Aldrich, St. Louis, MO) and 200 μL of 2M ammonium acetate (Sigma Aldrich, St. Louis, MO) pH 7, were added to 4 mCi (10 μL) of ^{89}Zr -oxalate (3D Imaging, Little Rock, AR). To the aforementioned mixture, 1 μmol of desferroxamine-conjugated nanoparticles [$\text{Df-PEG40-(SN-38)}_3$, Df-PEG40 , and $\text{Df}_4\text{-PEG40}$] (ProLynx LLC, San Francisco, CA), previously dissolved in deionized water (40 mg/mL), were added. The mixture was allowed to stand for 1 hour at 25°C. The solution was purified by size exclusion chromatography using a PD-10 desalting column (GE Healthcare, Little Chalfont, United Kingdom) and a saline solution served as the mobile phase.

Fractions of 1 mL were collected and measured for radioactivity in a dose calibrator (Capintec Inc., Florham Park, NJ). Radiochemical yield was calculated and based on the initial

amount of radioactivity. Radiochemical purity was determined using size-exclusion high-performance liquid chromatography (HPLC). The purified compound (20 μ L) was injected into a BioSep-SEC-S 3000 of 300 x 7.8 mm column (Phenomenex, Torrance, CA). Ultraviolet (UV) and radioactivity signals were monitored. Phosphate-buffered saline (PBS) was used as the mobile phase and the flow was maintained at 1 mL/min. In addition, instant thin layer chromatography (iTLC) was also used to monitor radiochemical purity. An aliquot (2 μ L) of the final solution was added to a glass microfiber chromatography paper impregnated with silica gel, iTLC-SG (Agilent Technologies, Santa Clara, CA), and added to a 10-mL tube containing ethylenediaminetetraacetic acid (EDTA).

B. μ PET/CT Imaging Studies

Animal Models

All animal studies were reviewed and approved by the University of California, San Francisco Institutional Animal Care and Use Committee (UCSF-IACUC). The experiments were conducted on immunocompromised mice, which had been implanted with various xenograft or PDX tumors. All injections and engraftments took place at the UCSF Cancer Center Preclinical Therapeutics Core, and the mice were transferred to the imaging suite at the UCSF Department of Radiology and Biomedical Imaging at China Basin.

NOD scid gamma (NSG) mice (Jackson Laboratory, Sacramento, CA), were injected with tumor cells into their flank or engrafted with a patient derived tumor. Two different xenograft

tumor models were used in these experiments, human MX-1 cell line derived breast cancer [20] and human HT-29 cell line derived colon cancer [21]. In addition, one study was performed on a PDX pancreatic tumor model (PDAC PC120).

Experiment Procedure

For the μ PET-CT imaging, the Siemens Inveon imaging system (Siemens, Munich, Germany) was utilized. The system is comprised of two independent scanners – the Inveon dedicated PET (D-PET) and the Inveon CT scanner [22].

Three separate studies were performed: (1) Assessment of the PK and BioD of ^{89}Zr –Df-PEG40-(SN-38)₃, ^{89}Zr –Df-PEG40, and ^{89}Zr –Df₄-PEG40 in mice bearing MX-1 xenograft tumors at 1, 24, 48, 72, 96, and 216 hours post-injection, (2) Assessment of the PK and BioD of ^{89}Zr –Df-PEG40-(SN-38)₃, ^{89}Zr –Df-PEG40, and ^{89}Zr –Df₄-PEG40 in mice bearing HT-29 xenograft tumors at 1, 24, 48, 72, 96, and 216 hours post-injection, and (3) Assessment of the PK and BioD of ^{89}Zr –Df₄-PEG40 in mice bearing pancreatic PDX tumors at 1, 4, 24, 72, 168, and 240 hours post-injection. Ex vivo BioD studies were performed for all of the mice after the final time point.

A total of 28 mice were used throughout these experiments: 12 MX-1 xenograft bearing mice (4 mice for each nanoparticle), 12 HT-29 xenograft bearing mice (4 mice for each nanoparticle) and 4 PDX tumor bearing mice.

Mice were anesthetized using isoflurane (Henry Schein Animal Health, Dublin, OH), followed by an intravenous tail injection of the designated nanoparticle (~7 nmol; 150 – 200 μCi

per mouse), followed by a saline flush (Hospira, Lake Forest, IL). One hour after administration, the mice were imaged, all four simultaneously. After the baseline imaging, the mice recovered and were re-anesthetized and imaged at the various time points mentioned above. Image acquisition times lasted for 30 minutes, 20 minutes for PET scans and 10 minutes for CT scans.

C. Image Processing

Image analysis was completed using the multimodal medical image processing software, AMIDE [23]. In vivo region of interest (ROI) quantitative analysis would provide the necessary data to assess the uptake of the radiolabeled nanoparticle. Cylinder shaped ROIs were used for the major organs (brain, heart, liver, and kidneys) and ellipsoid shaped ROIs for the various tumors. Once numerical data was extracted from the images, statistical analysis was performed using Microsoft Excel (Microsoft Corporation, Redmond, WA) and GraphPad Prism (GraphPad Software Inc., La Jolla, CA). Percent injected dose (%ID), percent injected dose per milliliter (%ID/mL), and t-test P-values for statistical relevance were the primary results acquired. For each study, time activity curves (TACs) were generated using GraphPad Prism.

D. BioD

In addition, nanoparticle data acquired via ROI quantification was compared to the results from a Hidex automatic gamma counting machine (Hidex, Turku, Finland) [24]. After the final time point, mice were euthanized and blood, organs (brain, bone, heart, kidney, liver, lung and spleen), as well as tumor tissue samples were excised, weighted, and counted. Ex vivo BioD

studies were performed to correlate and validate the accuracy of our in vivo ROI quantification. Percent injected dose per gram (%ID/g) and percent injected dose per organ (%ID/organ) were acquired using a known standard of the injected dose. Significance between samples was performed using the t-test.

Results

Nanoparticle radiolabeling reached greater than 90% yield and 99% purity for each of the three nanoparticles. iTLC and HPLC chromatograms can be seen in Figure 6. Such good labeling results allowed us to move forward with the in vivo preclinical model studies.

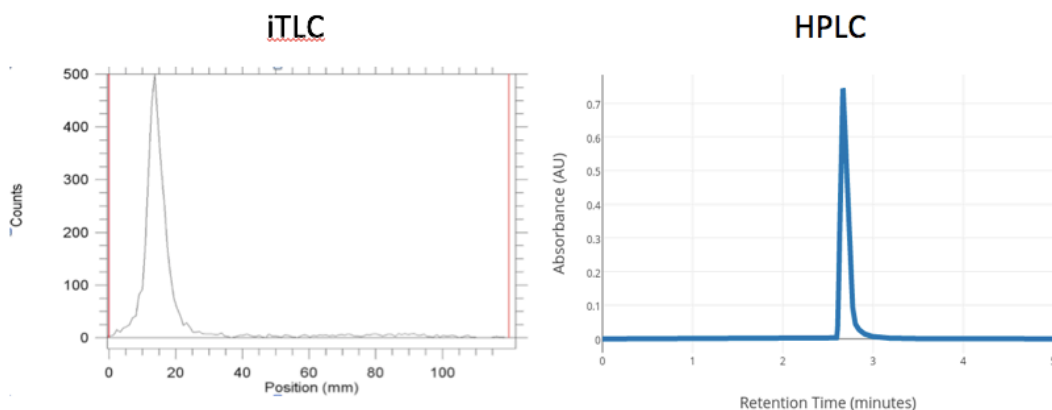


Figure 6: iTLC and HPLC chromatograms.

The PK studies of the different nanoparticles in MX-1 xenograft mice demonstrated similar distribution patterns. Post-injection, the nanoparticles circulate in the bloodstream, steadily accumulating within the tumor microenvironment. Little to no accumulation of the nanoparticles takes place within the major organs (Figure 7).

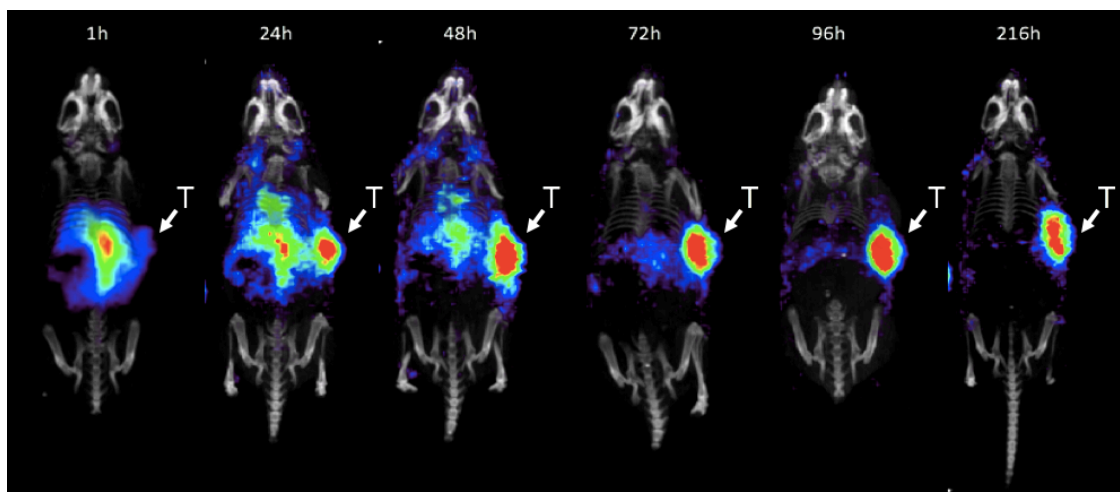


Figure 7: PK of ^{89}Zr -Df-PEG40-(SN-38)₃ in a mouse bearing an MX-1 xenograft tumor. Over time, the nanoparticle clears from the bloodstream and concentrates within the tumor microenvironment (T). This figure serves as a representative image of the in vivo PK for all of the nanoparticles.

Combined TACs for each nanoparticle in MX-1 tumor bearing mice are shown in Figure 8. When comparing the different nanoparticles over time, one can clearly see a steady accumulation followed by a plateauing of the concentration within the growing tumor, as well as clearance from all of the major organs (brain, heart, liver, and kidneys). Nanoparticle tumor concentrations appeared to reach a maximum at the 72-hour time point. These findings are consistent for all three versions of the nanoparticle.

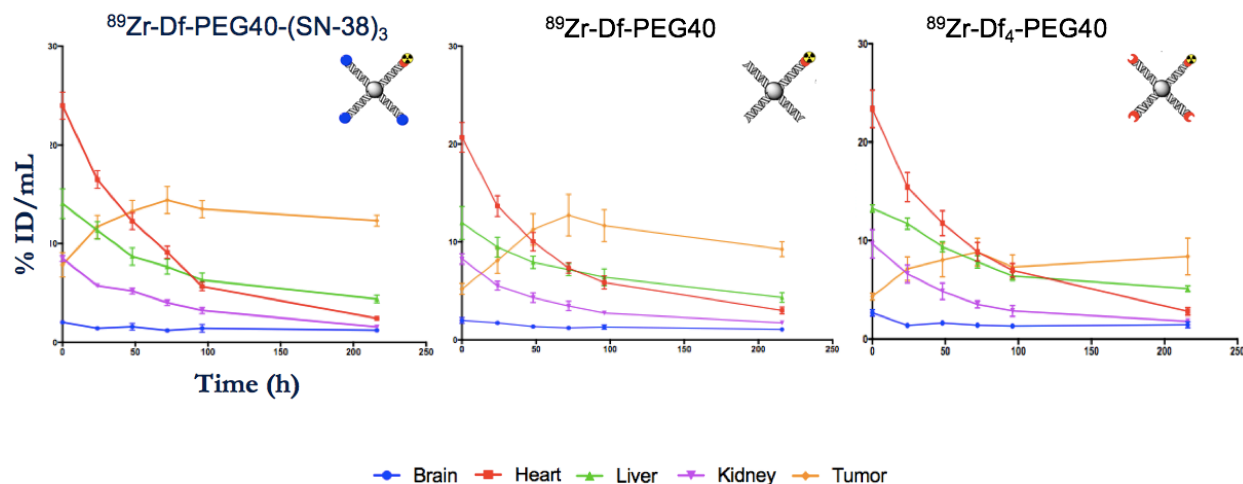


Figure 8: TACs for nanoparticle injections in mice bearing MX-1 tumors.

Following the same protocol, HT-29 xenograft bearing mice were injected with the same radiolabeled nanoparticles. TACs are shown in Figure 9. Results remained consistent for all three versions of the nanoparticle. When assessing the PK of the nanoparticles, one can clearly see a steady accumulation followed by a plateauing of the nanoparticle concentration within the growing tumor, as well as a clearance from all of the major organs (brain, heart, liver, and kidneys). Nanoparticle tumor concentrations appeared to reach a maximum at the 96-hour time point.

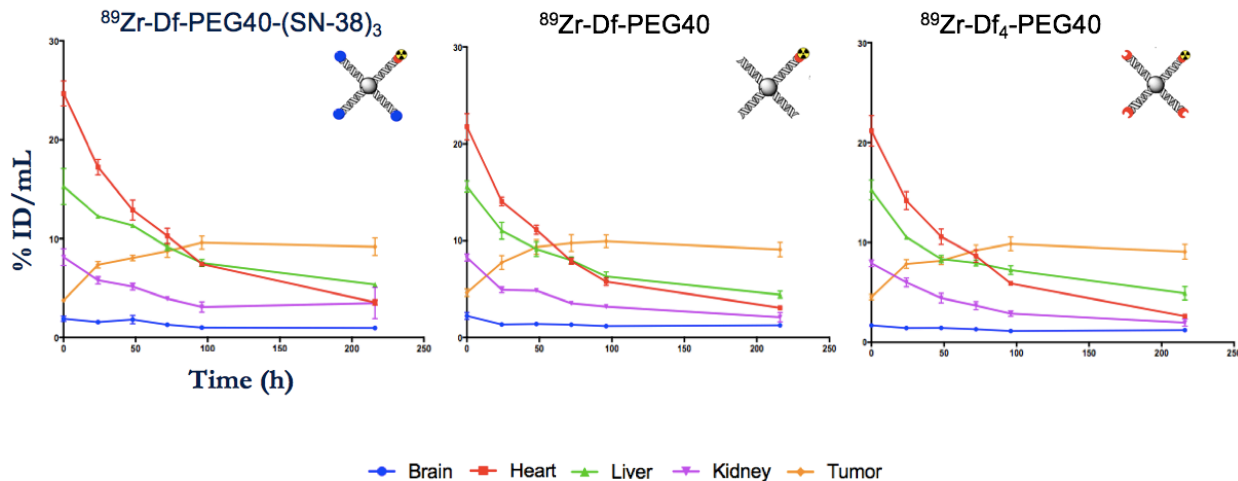


Figure 9: TACs for nanoparticle injections in mice bearing HT-29 tumors.

Nanoparticle uptake within the major organs was assessed across the six studies performed above (Figure 10). These graphs represent a compilation of all of the major organs (brain, heart, liver, and kidneys) and similar PK trends can be observed for all of them. The brains of the mice showed little to no uptake of the nanoparticle, while the hearts, livers, and kidneys showed decreasing levels of the nanoparticle over time. No significant differences ($P > 0.05$) were seen between the various curves.

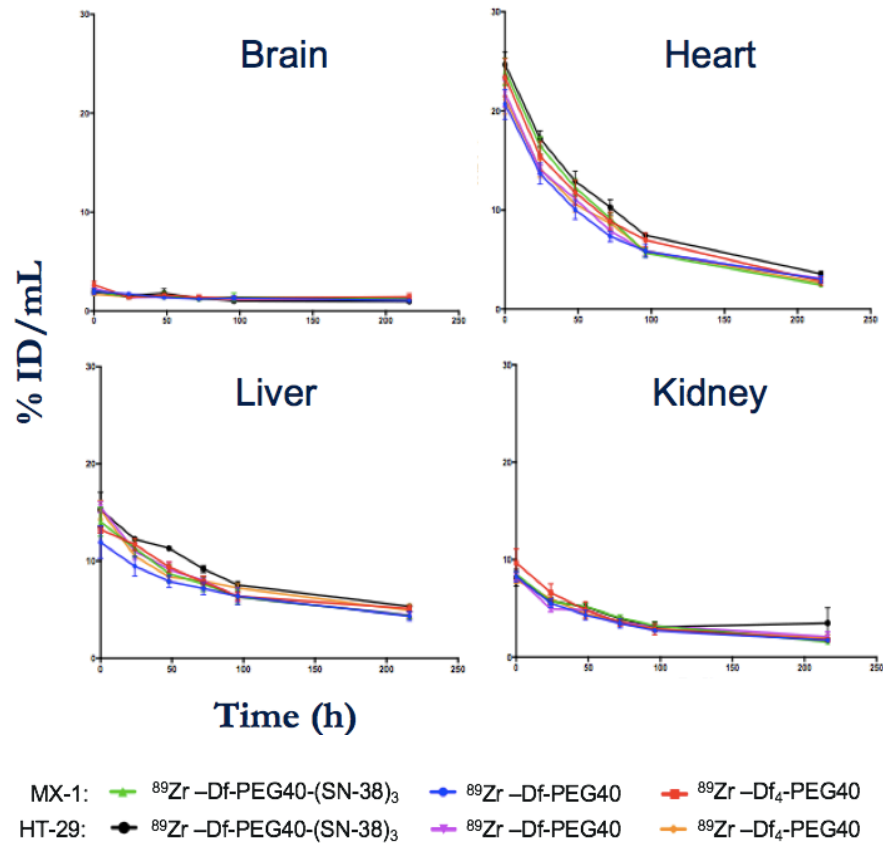


Figure 10: Major organ TACs.

The uptake of the various nanoparticles within the different tumors was assessed (Figure 11). Maximum uptake (5.81 to 18.14 %ID/mL) occurred around the 72-hr time point for most of the nanoparticles, with others reaching 96-hours. TACs demonstrate a steady rise and plateau of the nanoparticle concentrations within the tumors.

The nanoparticle results were compared by their accumulation in the two different xenograft tumors (Figure 12). Results for the imaging probes ^{89}Zr –Df-PEG40 and ^{89}Zr –Df₄-PEG40 showed no statistically different uptake ($P > 0.05$) when comparing the MX-1 tumor uptake versus the respective HT-29 tumor uptake. ^{89}Zr –Df-PEG40-(SN-38)₃, on the other hand showed

higher uptake in the MX-1 tumor when compared to its uptake in the HT-29 tumors ($P < 0.05$). Despite this difference, the overall shape of the curves remained the same.

We then looked at all of the nanoparticles and compared them by tumor type (Figure 13). Statistically significant differences ($P < 0.05$) in their uptake in the MX-1 xenograft tumors were observed. Nevertheless, the imaging probe ^{89}Zr -Df-PEG40 appeared to have a similar uptake when compared to the therapeutic version ^{89}Zr -Df-PEG40-(SN-38)₃. No statistically significant differences in the nanoparticle uptakes took place in the HT-29 tumors ($P > 0.05$), with the different nanoparticle curves appearing almost discernable.

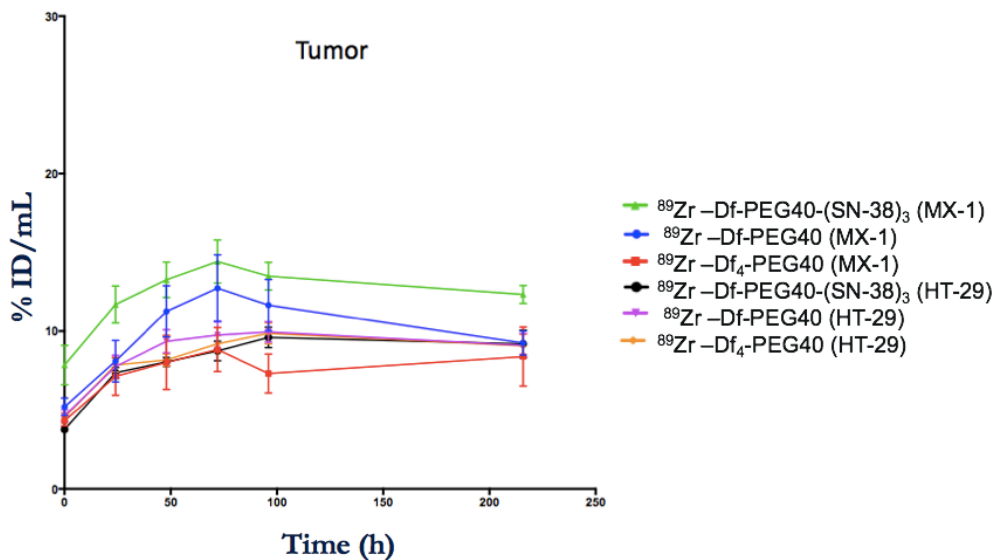


Figure 11: Combined MX-1 and HT-29 tumor TACs. Maximum %ID/mL occurred between the 72 and 96 hour time points, and ranged from 5.81 to 18.14 %ID/mL.

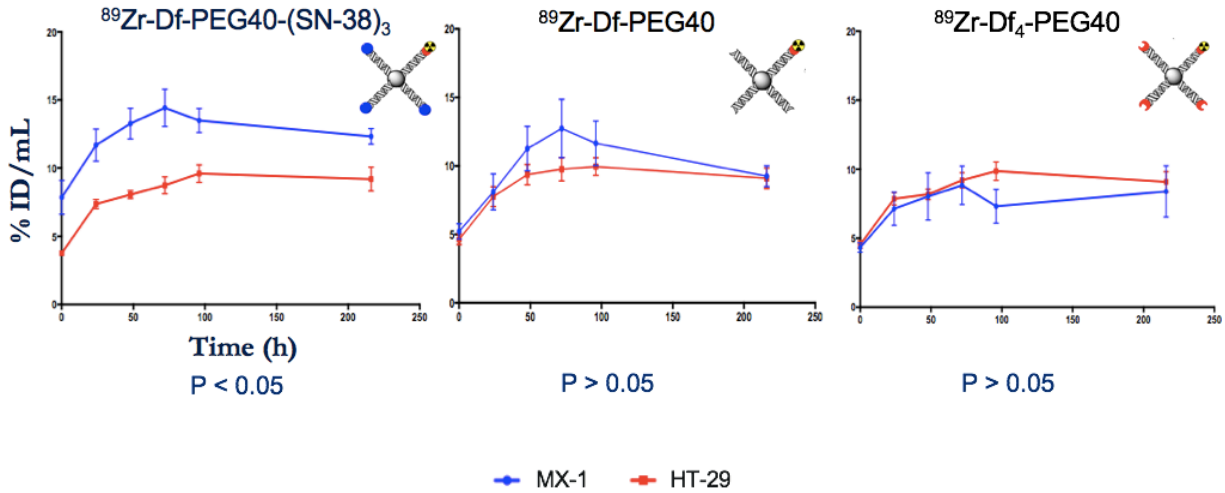


Figure 12: Combined TACs by nanoparticle type.

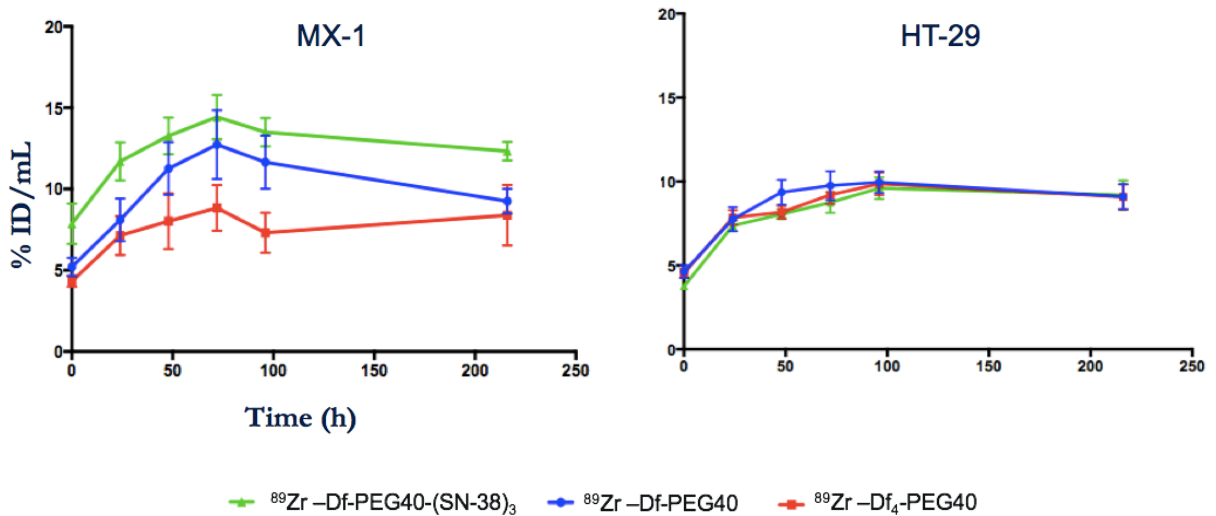


Figure 13: Combined TACs by tumor type.

The ex vivo BioD studies, performed after the final time point, reveal that regardless of the nanoparticle injected and of the xenograft tumor type, notable accumulation (%ID/g) takes place in the tumor tissues as well as in the spleens of the mice (Figure 14).

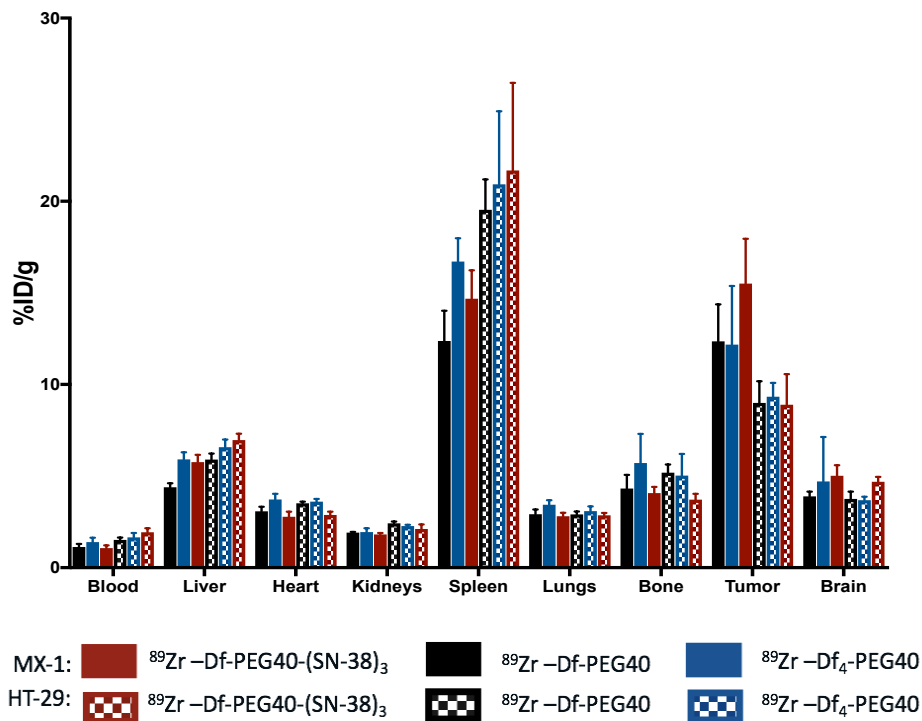


Figure 14: Ex vivo BioD (%ID/g).

When assessing the data from a different point of view, and looking at the overall organ and tumor uptake (%ID/organ), one can observe a similar trend and accumulation proportions as those seen in their respective TACs. Towards the last time point, the tumor and liver show the highest nanoparticle concentrations respectively (Figure 15), regardless of the nanoparticle construct assessed.

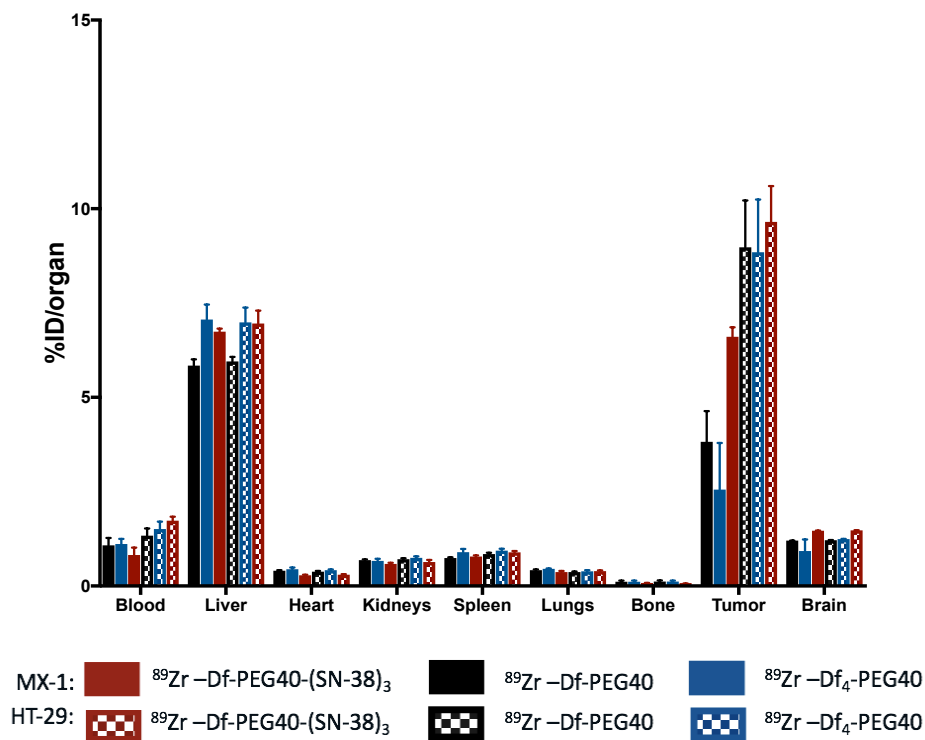


Figure 15: Ex vivo BioD (%ID/organ).

Results from the tumor ROIs of the final time point were directly compared to the results from the Hidex, automatic gamma photon counting machine. Results appear to be comparable, with insignificant statistical differences ($P > 0.05$) between the in vivo BioD and ex vivo BioD for the various tumor tissues (Figure 16), regardless of the nanoparticle construct assessed.

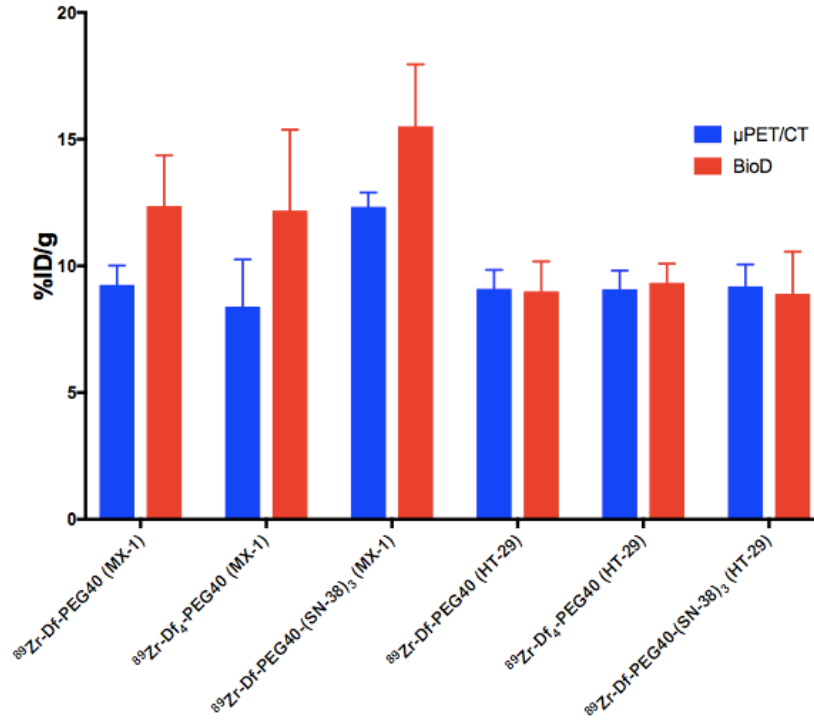


Figure 16: AMIDE ROI ($\mu\text{PET}/\text{CT}$) versus Hidex (BioD) tumor data comparison. ($P > 0.05$).

The uptake of $^{89}\text{Zr-Df}_4\text{-PEG40}$ was also evaluated in mice bearing a pancreatic PDX tumor (Figure 17). TACs show a steady accumulation followed by a plateauing of the nanoparticle concentration within the growing tumor, as well as a clearance from all of the major organs assessed (brain, heart, liver, and kidneys). Results from this study are comparable to those acquired from the xenograft tumor bearing mice.

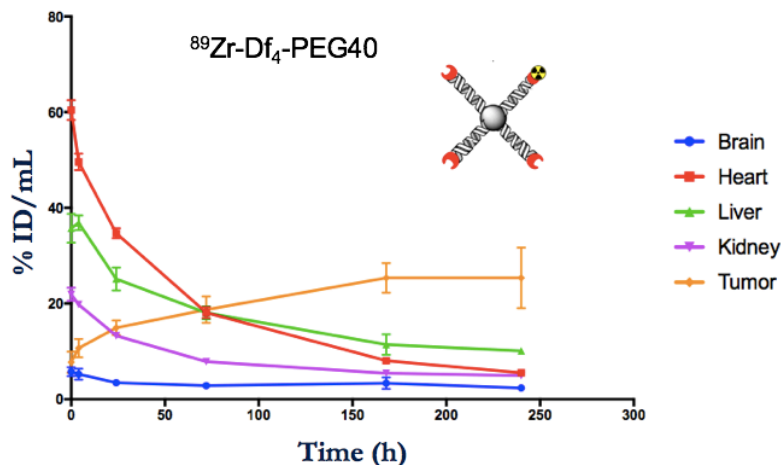


Figure 17: TACs for nanoparticle injections in mice bearing a pancreatic PDX tumor.

Discussion

The goal of this study was to assess the uptake of different versions of a novel nanoparticle, one with the integrated chemotherapeutic ^{89}Zr -Df-PEG40-(SN-38)₃, and two without, ^{89}Zr -Df-PEG40 and ^{89}Zr -Df₄-PEG40. The idea behind these specific experiments was to observe whether one, or even both non-therapeutic versions of the nanoparticle could predict the PK and BioD of the therapeutic version and serve as a viable imaging probe which can hopefully be transitioned into the clinic in the near future.

Regardless of the nanoparticle injected, or the xenograft tumor type present on the flank of the mice, all of the general TACs generated (Figure 8 & 9) showed similar results: a steady accumulation followed by a plateauing of the nanoparticle concentration within the growing tumor, as well as clearance from all of the major organs (brain, heart, liver, and kidneys) over time. Such results are consistent with the EPR effect [25]. Once the nanoparticles enter the tumor

microenvironment via the “leaky” vasculature, they accumulate and remain there due to poor lymphatic drainage [26]. Healthy vasculature, which does not suffer from enlarged endothelial pores, should display limited extravasation of the nanoparticles [27].

When comparing the curves on an organ-by-organ basis (Figure 10), general curve shapes roughly matched each other. For all of the experiments, the brains of the mice showed the smallest levels of uptake among all of the major organs assessed. We speculate that properly functioning blood-brain-barriers prevent nanoparticles from accumulating in the mice brains. Long-circulating nanoparticles in the bloodstream will repeatedly pass through the heart, until they accumulate within the tumor microenvironment or are either metabolized or excreted. As blood concentrations decrease over time, naturally so does the heart signal. Decreased blood concentrations also correlate with decreasing levels of glomerular filtration within the kidneys, which serves as the main mode of excretion of the nanoparticle. Despite PEG enhancing kidney removal, moderate levels of opsonization and removal by the reticuloendothelial system in the liver can still be observed. In fact, significant levels of the nanoparticles were still present in the liver towards the later time points. This non-target accumulation (hepatic uptake) appears to be a recurring limitation among most nanoparticle delivered chemotherapies [28].

In the generated tumor TACs (Figures 11 & 12), breakdown of the curves by nanoparticle type provided a substantial amount of information. Maximum %ID/mL occurred between the 72 and 96 hour time points, and ranged from 5.81 to 18.14 %ID/mL. Although ^{89}Zr -Df-PEG40-(SN-38)₃ showed varying accumulation levels ($P < 0.05$) when comparing its MX-1 and HT-29 uptake, the overall trend of the curves remained nearly similar. Differential accumulation can be attributed

to the heterogeneity of the vasculature and of the EPR effect between different tumors. On the other hand, uptakes of ^{89}Zr –Df-PEG40 and ^{89}Zr –Df₄-PEG40 showed no statistically significant differences ($P > 0.05$).

When breaking down the tumor uptake by xenograft tumor type (Figure 13), one can easily observe that both of the imaging probes assessed could be viable options for predicting tumor delivery of the therapeutic nanoparticle. Uptake curves within the MX-1 xenograft tumors were fairly comparable, with ^{89}Zr –Df-PEG40 resembling the therapeutic nanoparticle curve ($P > 0.05$), more than that of ^{89}Zr –Df₄-PEG40 ($P < 0.05$). ^{89}Zr –Df-PEG40-(SN-38)₃ showed more variability with ^{89}Zr –Df₄-PEG40 than with ^{89}Zr –Df-PEG40. Statistically significant differences in the nanoparticle uptake in the MX-1 xenograft tumors may warrant a repeat experiment in the near future. On the other hand, TACs for the three nanoparticles within HT-29 tumors were almost indiscernible. What this analysis ultimately reveals is that there is no PK or BioD impact from integrating more than one radiolabel onto the nanoparticle. Increasing the radiolabeling per nanoparticle would essentially allow us to decrease the number of nanoparticles needed, therefore decreasing the cost of this screening process.

Ex vivo BioD studies showed significant tumor and spleen tissue accumulation (Figure 14). Non-specific accumulation of the nanoparticles within the spleen can be accounted for by the spleen's role in the reticuloendothelial system and small overall size relative to the other organs. When accounting for whole organ accumulation, and not normalizing the data per gram of tissue, results match those of the TACs (Figure 15). At the later time points, significantly higher uptake

and retention of the nanoparticle take place in the tumor relative to the other organs, indicative of the EPR effect taking place within the tumors.

Results from the tumor ROIs drawn on the μ PET/CT images were compared to those from the ex-vivo BioD study (Figure 16). The results acquired did not show any statistically significant differences ($P > 0.05$), further supporting all of the findings we have acquired so far in these assessments via ROI quantification. Consistent outcomes confirm the validity of the non-invasive technique, and its advantage in terms of practicality and minimizing animal use.

It has been reported that cell-line derived xenograft tumor models oftentimes underplay the efficacy of various oncologic treatments. Cell-line derived xenograft tumors suffer from a lack of predictable relationship between therapeutic responses in preclinical models when compared to responses in human trials, due in part to its inability to accurately represent a tumor microenvironment [29]. PDX tumors, on the other hand, demonstrate varied vasculature all the while providing an even more hypoxic environment than simple xenografts. Nevertheless, good xenograft tumor results have prompted us to evaluate the PK and BioD of the nanoparticles in PDX tumor bearing mice.

The TACs generated for the pancreatic PDX tumor bearing mice (Figure 17), show a similar pattern to the cell-line derived xenograft bearing mice. A steady accumulation followed by a plateauing of the nanoparticle concentration within the growing tumor, as well as a clearance from all of the major organs (brain, heart, liver, and kidneys) over time. Again, these results are

indicative of the EPR effect for tumor accumulation, and further reinforce all of the conclusions made so far.

This star-shaped nanoparticle offers PK and BioD advantages over already approved nanocarriers such as liposomes. Organic liposomal nanoparticles are very attractive, not only due to the possibility of delivering high therapeutic doses, but the interchangeability of the phospholipids within the bilayer allows scientists to optimize its efficacy [30]. Nevertheless, the biggest drawback from this therapy remains the liposomes' large size. Current liposome products tend to range around 100 nm [31]. As previously mentioned, tumor vascular pores have a wide distribution in size (12 - 700 nm). This means that tumors which have pores ranging from 12 to 100 nm may not benefit from any form of liposomal treatment. Use of smaller nanoparticles, closer to the minimal pore size, would extravasate from a wider range of tumor vasculature and travel further within the tumor [32], thus having the potential of being efficacious in numerous tumor types. With Df-PEG40 having a size of 20 nm, this therapy would be able to cater to an even wider tumor vascular pore range and overcome some of the limitations of liposomes.

On the other hand, antibody drug conjugates (ADCs) are an even smaller delivery molecule than our nanoparticle in question, with antibody sizes ranging around 12 nm [33]. Different delivery mechanisms have comparable tumor uptake and similar reduced systemic effects. Nevertheless, smaller carriers often have significant non-specific uptake due to their ability to pass through healthy vascular pores (≤ 12 nm). In addition, ADC's undergo active targeting which, although more efficacious for the original tumor, may not be beneficial for the metastases due to significant inter-tumor heterogeneity [34]. As a cancer disseminates, its metastases evolve

independently of the original tumor; different mutations lead to different receptor overexpression, resulting in varying levels of affinity when it comes to ADCs. Moreover, as with all antibody-based therapies, ADC's face issues regarding immunogenicity. Recognition of the crystallizable (Fc) region by the host immune system could severely affect an ADC's overall PK and BioD, thus impacting treatment delivery [35]. Several leading experts point to the idea that particle accumulation within the tumor microenvironment is often mediated by its physico-chemical properties, and is a more powerful predictor than active targeting [17]. As a result, we remain confident in the practicality of this novel, passively targeting, Df-PEG40 nanotherapy delivery.

Which patients will respond and benefit the most from this new form of chemotherapy delivery is extremely dependent upon the specifics of the tumor vasculature. It is important to keep in mind that cancer is particularly heterogeneous, and that not all cell types respond in the same manner (in terms of levels of gene expression such as VEGF) when exposed to hypoxia [6, 36]. This often leads to varied micro-vascular densities (MVD) and heterogeneous endothelial pore sizes within the tumor vasculature. Other possible barriers with the nanoparticle delivery system include tumor viable rims (which often surround a solid tumor's hypoxic core) as well as newly formed metastases which may rely on vessel co-option rather than neo-angiogenesis for nutrient supply. Vessel co-option constitutes taking advantage of the adjacent healthy tissue's vascular supply [37]. Those vessels do not suffer from abnormally shaped endothelial pores (≤ 12 nm), meaning that the nanoparticle would not be able to pass through, leaving the growing mass of cells without any administered treatment. Moreover, patients who have undergone antiangiogenic therapy (i.e. bevacizumab) and have undergone a normalization of the tumor vasculature may not benefit from this nanoparticle delivery system. By pruning aberrant vessels and decreasing the

leakiness of the tumor vasculature, antiangiogenics and vascular disrupting agents have impacted the potential efficacy of this form of treatment. [38]. These potential limitations confirm the premise behind the idea of using the nanoparticle without any chemotherapy (^{89}Zr –Df-PEG40 or ^{89}Zr –Df₄-PEG40) as a form of screening process to assess whether a patient, and which of their tumors, may respond positively to this form of chemotherapy delivery.

Conclusion

The nanoparticles were successfully labeled with ^{89}Zr and the final products were obtained with purity higher than 99%. $\mu\text{PET}/\text{CT}$ imaging studies revealed similar PK of the nanoparticles within various pre-clinical murine models. A steady accumulation followed by a plateauing of the nanoparticle concentrations within the growing tumors, as well as a clearance from all of the major organs (brain, heart, liver, and kidneys). $\mu\text{PET}/\text{CT}$ PK results were confirmed with ex vivo BioD assessments.

As of now, we will explore the PK of the radiolabeled nanoparticles in a pre-clinical metastatic cancer model. Beyond xenograft and PDX tumors, metastatic tumor models will allow us to evaluate the behavior of the nanoparticle within even more varied vasculature. Our goal is to complete the necessary preclinical proof-of-concept experiments so as to transition to clinical trials, with the imaging probes playing a major role in assessing nanoparticle accumulation and predicting potential patient benefit.

References

- [1] Liang et al. (2011). Circumventing Tumor Resistance to Chemotherapy by Nanotechnology. *Methods Mol Biol.* 2010;596:467-88.
- [2] Chopra et al. (2016). Chemotherapy-Induced Adverse Drug Reactions in Oncology Patients: A Prospective Observational Survey. *Indian J Med Paediatr Oncol.* 2016 Jan-Mar; 37(1): 42-46.
- [3] Lisy, K., & Peet, D.J. (2008). Turn Me On: Regulating HIF Transcriptional Activity. *Cell Death Differ.* 2008 Apr;15(4):642-649.
- [4] Hillen, F., & Griffioen, A. (2007). Tumor Vascularization: Sprouting Angiogenesis and Beyond. *Cancer Metastasis Rev.* 2007 Dec; 26(3-4);489-502.
- [5] Nagy, J., & Dvorak, H. (2012). Heterogeneity of the Tumor Vasculature: The Need for New Tumor Blood Vessel Type-Specific Targets. *Clin Exp Metastasis.* 2012 Oct;29(7):657-662.
- [6] Majmundar et al. (2010). Hypoxia-Inducible Factors and the Response to Hypoxic Stress. *Mol Cell.* 2010 Oct 22; 40(2):294-309.
- [7] Noy, R., & Pollard, J. (2014). Tumor-Associated Macrophages: From Mechanisms to Therapy. *Immunity.* 2014 Jul 17;41(1):49-61.
- [8] Mantovani et al. (2008). Cancer-Related Inflammation. *Nature.* 2008 Jul 24; 454(7203):436-444.
- [9] Zhang, Y., et al. (2017). DT-13 Ameliorates TNF- α -Induced Vascular Endothelial Hyperpermeability via Non-Muscle Myosin IIA and Src/PI3K/Akt Signaling Pathway. *Front Immunol.* 2017; 8: 925.
- [10] Petrache et al. (2003). The Role of Microtubules in Tumor Necrosis Factor- α -Induced Endothelial Cell Permeability. *Am J Respir Cell Mol Biol.* 2003 May;28(5):574-581.
- [11] Hashizume et al. (2000). Openings Between Defective Endothelial Cells Explain Tumor Vessel Leakiness. *Am J Pathol.* 2000 Apr; 156(4): 1363-1380.
- [12] VanHorsen et al. (2006). TNF-Alpha in Cancer Treatment: Molecular Insights, Antitumor Effects, and Clinical Utility. *Oncologist.* 2006 Apr; 11(4):397-408.
- [13] Nichols, J., & Bae, Y. (2014). EPR: Evidence and Fallacy. *J Control Release.* 2014 Sep 28;190:451-464.
- [14] Qi et al. (2017). Co-delivery Nanoparticles of Anti-Cancer Drugs for Improving Chemotherapy Efficacy. *Drug Delivery.* 24(1), 1909-1926.

- [15] Jurj et al. (2017). The New Era of Nanotechnology, An Alternative to Change Cancer Treatment. *Drug Des Devel Ther.* 2017; 11: 2871-2890.
- [16] Nguyen, K. (2011). Targeted Nanoparticles for Cancer Therapy: Promises and Challenges. *J Nanomedic Nanotechnol* 2:103e.
- [17] Danhier, F. (2016). To Exploit the Tumor Microenvironment: Since the EPR Effect Fails in the Clinic, What is the Future of Nanomedicine? *J Control Release.* 2016 Dec 28;244(Pt A):108-121.
- [18] Lai et al. (2017). Current Status and Perspectives of Patient-Derived Xenograft Models in Cancer Research. *Journal of Hematology & Oncology.* 2017, 10:106.
- [19] Heskamp et al. (2017). 89Zr-Immuno-Positron Emission Tomography in Oncology: State-of-the-Art 89Zr Radiochemistry. *Bioconjugate Chem.* 2017, 28, 2211-2223.
- [20] Jin et al. (2011). XLN306 Induces Apoptosis in human Breast Carcinoma MX-1 Cells. *Acta Pharmaceutica Sinica B.* 1(2): 84-88.
- [21] Limami et al. (2011). HT-29 Colorectal Cancer Cells Undergoing Apoptosis Overexpress COX-2 to Delay Ursolic Acid-Induced Cell Death. *Biochimie.* 93(4); 749-757.
- [22] Siemens (2008). Inveon, No Limits on Discovery. Retrieved: Thursday, August 30th, 2018. (http://www.microscopy.wisc.edu/files/micro/Inveon_Brochure.pdf)
- [23] Loening, A., & Gambhir, S. (2003). AMIDE: a Free Software Tool for Multimodality Medical Image Analysis. *Mol Imaging.* 2003 Jul; 2(3):131-7.
- [24] Hidex (2017). Hidex AMG Automatic Gamma Counter. Retrieved: Thursday, August 30th, 2018. (http://hidex.com/wp-content/uploads/2017/11/Hidex_AMG_WEB_0903_2017.pdf)
- [25] Maeda, H. (2001). The Enhanced Permeability and Retention (EPR) Effect in Tumor Vasculature: The Key Role in Tumor-Selective Macromolecular Drug Targeting. *Adv Enzyme Regul.* 2001;41:189-207.
- [26] Fang et al. (2011). The EPR Effect: Unique Features of Tumor Blood Vessels for Drug Delivery, Factors Involved, and Limitations and Augmentation of the Effect. *Adv Drug Deliv Rev.* 2001 Mar 18;63(3): 136-151.
- [27] Iyer et al. (2006). Exploiting the Enhanced Permeability and Retention Effect for Tumor Targeting. *Drug Discov Today.* 2006 Sep; 11(17-18): 812-818.
- [28] Nichols, J., & Bae, Y. (2012). Odyssey of a Cancer Nanoparticle: From Injection Site to Site of Action. *Nano Today.* 2012 Dec 1;7(6):606-618.

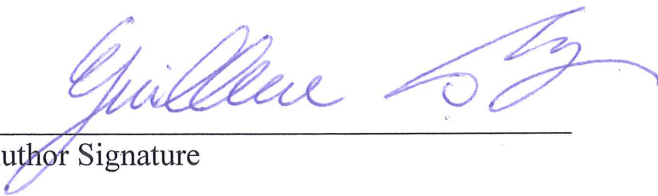
- [29] Pearson et al. (2016). Patient-derived xenograft (PDX) Tumors Increase Growth Rate with Time. *Oncotarget*. 2016 Feb, 7(7):7993-8005. Doi: 10.18632/oncotarget.6919.
- [30] Zhang, H. (2016). Onivyde for the Therapy of Multiple Solid Tumors. *Onco Targets and Therapy*. 2016 6:9, 3001-3007.
- [31] Bulbake et al. (2017). Liposomal Formulations in Clinical Use: An Updated Review. *Pharmaceutics*. 2017 Mar 27;9(2). pii: E12.
- [32] Wilhelm et al. (2016). Analysis of Nanoparticle Delivery to Tumours. *Nat Rev Mat*. 2016;1:1-12.
- [33] Lammers et al. (2012). Drug Targeting to Tumors: Principles, Pitfalls and (Pre-) Clinical Progress. *J Control Release*. 2012 Jul 20;161(2):175-187.
- [34] Howard et al. (2016). Antibody-Drug Conjugates and Other Nanomedicines: The Frontier of Gynaecological cancer treatment. *Interface Focus*. 6: 20160054.
- [35] Hock et al. (2015). Immunogenicity of Antibody Drug Conjugates: Bioanalytical Methods and Monitoring Safety Strategy for a Novel Therapeutic Modality. *AAPS J*. 2015 Jan; 17(1): 35-43.
- [36] Chi et al. (2006). Gene Expression Programs in Response to Hypoxia: Cell Type Specificity and Prognostic Significance in Human Cancers. *PLoS Med*. 2006 Mar;3(3):e47.
- [37] Donnem et al. (2013). Vessel co-option in primary human tumors and metastases: an obstacle to effective anti-angiogenic treatment? *Cancer Med*. Aug; 2(4): 427-436.
- [38] Jain, R. (2005). Normalization of Tumor vasculature: An Emerging Concept in Antiangiogenic Therapy. *Science*. 2005 Jan 7;307(5706):58-62.

Publishing Agreement

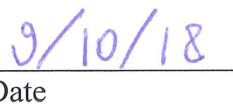
It is the policy of the University to encourage the distribution of all theses, dissertations, and manuscripts. Copies of all UCSF theses, dissertations, and manuscripts will be routed to the library via the Graduate Division. The library will make all theses, dissertations, and manuscripts accessible to the public and will preserve these to the best of their abilities, in perpetuity.

Please sign the following statement:

I hereby grant permission to the Graduate Division of the University of California, San Francisco to release copies of my thesis, dissertation, or manuscript to the Campus Library to provide access and preservation, in whole or in part, in perpetuity.



Author Signature



Date